Dynamics and Spatial Organization of Endosomes in Mammalian Cells

Chinmay Pangarkar, Anh Tuan Dinh, and Samir Mitragotri*

Department of Chemical Engineering, University of California Santa Barbara, Santa Barbara, California 93106, USA

(Received 8 February 2005; published 5 October 2005)

We combine particle tracking and stochastic simulations to analyze the dynamics and organization of early endocytic vesicles in mammalian cells. At short time scales ($<10^1$ sec) vesicles exhibit 1D symmetric bidirectional motor-driven transport on microtubules such that the mean squared displacement (MSD) scales as $t^{3/2}$, but the MSD shows a crossover to facilitated diffusion at longer times ($>10^1$ sec). Facilitated diffusion results in rapid equilibration of vesicles on microtubules. The asterlike organization of microtubules causes perinuclear accumulation of vesicles despite symmetric transport.

DOI: 10.1103/PhysRevLett.95.158101 PACS numbers: 87.16.Dg, 87.16.Ka, 87.16.Nn, 87.16.Tb

Endocytosis is the primary mechanism used by mammalian cells for internalizing extracellular entities. Endocytic vesicles (endosomes), which contain the internalized entities, originate at the cell periphery and eventually concentrate near the nucleus [1–3]. This perinuclear accumulation of endosomes is an indispensable step in proper processing and disposal of most internalized entities. It is generally thought that perinuclear accumulation of subcellular vesicles, such as endosomes, is achieved by biased, motor-driven transport [4,5]. In this Letter, we show, using skin fibroblasts as a model cell line, that endosomes exhibit *symmetric unbiased* transport on microtubules and, surprisingly, still accumulate in the perinuclear region within 10–45 min. We report on the origin of this phenomenon and provide a quantitative explanation for the time scales of accumulation. Our experimental data and stochastic simulations show that symmetric unbiased transport on microtubules is an effective strategy used by mammalian cells to control the spatial organization of endosomes and possibly a broader family of subcellular organelles.

Endosomes are highly mobile structures, which continually interact with each other and with other organelles. Their transport is orchestrated by a network of tubulelike polarized filamentous polymers 25 nm in diameter, known as microtubules (MTs). MTs radiate out from a perinuclear MT organizing center (MTOC), forming an asterlike structure [Fig. 1(a)]. Movements on MTs are powered by motor proteins of the kinesin and dynein families, which move the vesicles to the plus ends (towards cell periphery) and to the minus ends of MTs (towards cell nucleus), respectively, [6]. Conceptually, the vesicles can be viewed as discrete particles that switch stochastically between free diffusion in cytosol and directed movements on MTs [5,7] [Fig. 1(b)]. The frequency, directionality, and persistence of the directed movements are controlled by complex interactions between vesicle-bound motors, regulatory proteins, and neighboring microtubules. At a single endosome level, MT-based transport can be fully characterized by the parameters shown in Fig. 1(b) [8], which have been quantified in certain cases. At a whole-cell level, studies have qualitatively shown that endosomes accumulate in the perinuclear region. However, the link between the transport parameters of endosomes and their spatial distribution has not been established and it is generally portrayed that some sort of biased motion (for example, $v_- > v_+$) is responsible for perinuclear accumulation of endosomes.

We employ a combined experimental and computational approach to understand the relationships between the parameters in Fig. 1(b) and the spatial organization of endosomes at various times. Using fluorescence microscopy we tracked movements of single endosomes and extracted parameters in Fig. 1(b). These parameters were then used in conjunction with stochastic simulations to establish the connection between particle dynamics at the discrete level and spatiotemporal evolution of endosomal distribution at the whole-cell level, which we also measured experimentally at various times.

Endosomes in cultured human skin fibroblasts were fluorescently labeled by three different endocytic markers,

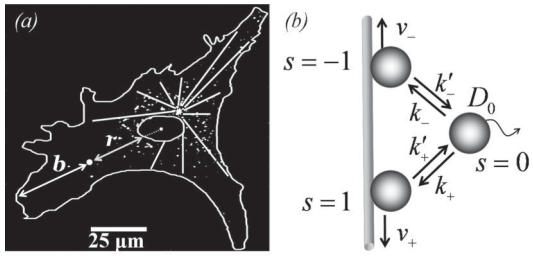

FIG. 1. (a) Fluorescent micrograph of a skin fibroblast incubated with fluorescent dextran, shows perinuclear accumulation of vesicles at 15 min postincubation (See Ref. [9] for more images). A cartoon of MT structure is superimposed. The coordinates used to locate vesicles are also shown—r and $\eta = r/(r + b)$. (b) A schematic showing the multiple states of a vesicle—(i) $s = 0$: freely diffusing with diffusivity D_0, (ii) $s = 1$: bound to MT, plus end movement with speed v_+ and (iii) $s = -1$: bound to MT, minus end movement with speed v_-. Binding/unbinding rates are described by first-order rate constants $k_\pm$ and $k'_\pm$, respectively, which, in turn, determine the fraction f of particles undergoing directed transport at a given time, $f = \frac{K_+ + K_-}{K_+ + K_- + 1}$, $K_+ = k_+/k'_-$ and $K_- = k_-/k'_-$.

TABLE I. Transport properties of different endocytic markers measured from single-particle tracking data. L, the mean length of MTs was measured to be 30 μm.

Marker	Dextran	LDL	PEI-DNA
Time of equilibration (min)	10-15	30-45	45-75
Duration of steady state (min)	45	60	180
Mean time on MT, t^{on}(sec)	3.1	3.8	3.0
Mean v (μm/ sec)	0.35	0.32	0.33
Mobile fraction, f	0.5 ± 0.08	0.4 ± 0.1	0.2 ± 0.07
k', $s^{-1}[1/t^{on}]$	0.32	0.263	0.33
k, $s^{-1}[fk'/2(1-f)]$	0.16 ± 0.1	0.088 ± 0.06	0.041 ± 0.03
D^{eff}(μm^2/ sec)	0.19 ± 0.03	0.16 ± 0.4	0.07 ± 0.02

namely, dextran (a fluid phase marker), low-density lipoprotein (LDL) (a colloidal ligand that is internalized via a specific receptor on the cell surface), and PEI-DNA (a particulate complex of DNA and a cationic polymer polyethylenimine, used widely for gene delivery). These markers differ widely in their interactions with the cell membrane (see Ref. [9], Sec. B for a discussion of their endocytic fate).

We followed the movements of intracellular vesicles containing one of the three markers at different times postincubation using fluorescence microscopy. The entities we treat as vesicles are either early or late endosomes. This was confirmed by immunolabeling vesicles with a lysosomal marker (see Ref. [9], Sec. B). Fluorescence time-lapse videos 1–2 min long at 1 frame per sec were used to obtain the trajectories of about 400 vesicles in different cells. The following quantities were calculated for each trajectory: (i) frame to frame speed v, (ii) direction of motion (minus or plus end) for each step, and (iii) angle of motion with respect to the initial step. Based on these measurements, events of directed vesicle transport on the microtubules were detected. Only a fraction $f(\approx 0.2$–$0.5)$ of vesicles was found to exhibit rapid directed transport ($0.2\ \mu\text{m/sec} < v < 2\ \mu\text{m/sec}$) during the acquisition time, while others hardly moved (cf. the quantity f in Table I).

All the MT-based trajectories are found to be linear, bidirectional and oriented along the MT network [Fig. 2(a)]. When active trajectories are resolved into radial and orthoradial components, the total mean squared displacement is almost equal to its radial component, showing the dominance of radial motion over orthoradial motion. Surprisingly, the measured velocities of plus and minus end-directed steps showed almost identical exponential distributions, irrespective of spatial location, time, and marker (Fig. 3). The distribution of run lengths in either direction was also found to be indistinguishable (Fig. 3, inset). The exponential distribution of run lengths indicates that unbinding is indeed a first-order kinetic process [10] (cf. captions of Figs. 1 and 3). The fractions of vesicles moving towards plus and minus ends of MTs were also found to be approximately equal (0.48:0.52 for PEI-DNA and 0.50:0.50 for dextran). Thus, within the range of experimental errors, we conclude that MT-dependent transport of endosomes at single-particle level is *bidirectional, symmetric* (in an ensemble-average sense) and *one dimensional*.

At the whole-cell level, we calculated the average local concentration of fluorescently labeled vesicles, $c(r, t)$ (#vesicles/μm^2) as a function of distance r from the nuclear boundary [cf. Figure 1(a)] at various times postincubation. Immediately after internalization, the vesicles were distributed uniformly over the entire cell surface [Fig. 4(a), ●]. However, at longer times, vesicles accumulated around the nucleus [Fig. 4(a)—□, △, ○]. This asymmetric distribution was observed to persist for a certain period of time until it was changed by late endocytic events (cf. Table I). To capture the 1D nature of MT-based transport we transformed $c(r, t)$ to the η coordinate defined in Fig. 1(a). η represents the fractional position of a vesicle between the nuclear membrane and the cell membrane. Considering that a vesicle is confined to move linearly along neighboring microtubules, the domain $\eta = [0, 1]$ represents the space that can be explored by a vesicle. $p(\eta, t)$ represents the probability of a vesicle being at a

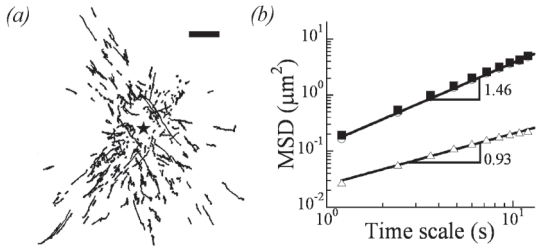

FIG. 2. Confinement of vesicle motion to one dimension. (a) Trajectories of 350 actively transported vesicles are plotted such that the geometric center of the nucleus of the parent cell is shifted to the origin (star). Scale bar is 20 μm. (b) Mean squared displacements averaged over all active trajectories, for the whole trajectory (■) and radial (○) and orthoradial (△) projections of the trajectory. Mean squared displacements were fitted to $\langle r^2 \rangle = at^{\gamma}$ separately for the radial and orthoradial components and, respectively, yielded $\gamma = 1.46$ and 0.93 showing directed transport in radial direction and diffusive transport in the orthoradial direction. The orthoradial diffusion coefficient was estimated to be 0.009 μm^2/ sec.

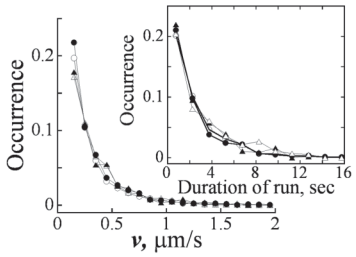

FIG. 3. Distribution of frame to frame speeds in the plus (solid) and minus (open) directions for dextran (triangles) and PEI-DNA (circles). Inset: Distribution of run lengths in the plus and minus directions (same legend) is also identical. These distributions are fitted to an exponential function to obtain $\langle v_+ \rangle = \langle v_- \rangle = \langle v \rangle = 0.33\ \mu\text{m/sec}$, ($r^2 = 0.96$) and $k'_+ = k'_- = k' = 0.34\ \text{sec}^{-1}$ ($r^2 = 0.99$). See Ref. [9], Sec. F for a comparison with other systems in literature.

distance η, at time t. The initial uniform distribution was then found to map to a linear curve $p(\eta) = 2\eta$, [● in Fig. 4(b)]. Interestingly, for all markers, the steady state asymmetric distributions (□, △, and ○) in r space were transformed to *uniform* distributions over $\eta = [0.1, 0.9]$. The apparent perinuclear accumulation of vesicles is actually due to the anisotropic, asterlike organization of MTs. A slight reduction in $p(\eta, t)$ near the cell membrane ($p < 0.05$) is attributed to inaccuracies in coordinate transformation from r to η caused by nonconvex cell geometry. Similarly, the interval $\eta = [0, 0.1]$ maps to a region of 2 μm width around the nucleus, where overcrowding of organelles probably leads to exclusion of vesicles from the perinuclear region (see Ref. [9], Sec. C).

Further supporting evidence for one-dimensional vesicular confinement and equilibration along the MTs is shown in Fig. 4(d), where concentrations of microtubules and vesicles are plotted. These data show that both decay with very similar profiles and confirm that vesicles are uniformly distributed on MTs.

A clear picture now emerges that the apparent accumulation of endosomes near the nucleus is a result of uniform distribution of endosomes on MTs. A question remains how the ballistic motion of vesicles on a short time scale (1–10 sec), leads to a uniform distribution after long times (10–60 min). Specifically, how are the parameters k, k', v, and D_0 related to the time scale at which distribution achieves steady state. Since particle tracking experiments cannot be performed for 30 min, we used stochastic simulations to answer this question. The simulations closely mimicked cellular conditions, including cell geometry, organization, and dynamic instability of MTs (see Ref. [9], Sec. D). Vesicles were allowed to switch stochastically between diffusion and directed transport just as in real cells. The binding/unbinding rate constants and distributions of motor speeds were directly adapted from data reported in Fig. 3. MSDs and whole-cell endosome distributions were generated for up to 60 min. At the whole-cell level, simulated vesicle distributions agreed well with experimental observations (see Fig. 4 in Ref. [9]), thus lending further support to experimental observations.

A comparison between the predicted MSD and the measured MSD is shown in Fig. 5(a). At short times ($t < 1$ sec), simulations show that vesicle motion is ballistic, as also seen in experiments (t^γ, $\gamma \approx 1.5$–2). However, at long times ($t > 10$ sec), simulations and theory show that vesicle motion exhibits diffusive scaling (t^1) and may be described by an effective diffusive coefficient, D^{eff}. Over short time scales, vesicles experience limited runs such that mean velocity is nonzero and directional. However, at long times, vesicle motion is averaged over several random

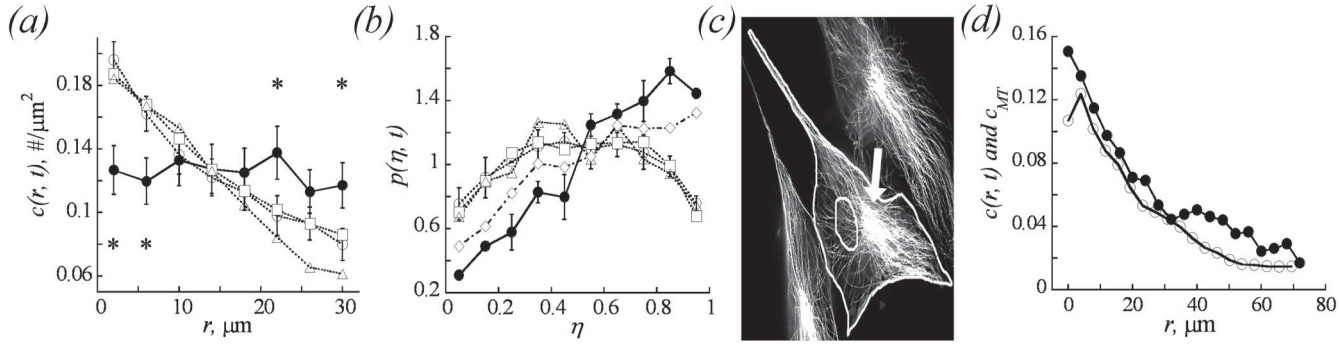

FIG. 4. (a) Concentration of vesicles $c(r, t)$. (i) PEI-DNA vesicles at short time (12–30 min postincubation, ●). Similar curves were observed for other vesicles and are not shown for clarity, (ii) Distribution of dextran (□) at 10–30 min, LDL (△) at 30–150 min, and PEI-DNA (○) at 60–180 min postincubation. Over these time periods, the distribution does not change. Asterisks mark the abscissae where short time data (●) are statistically different from long time data (○), $p < 0.05$. (b) Distribution of vesicles $p(\eta, t)$. PEI-DNA containing vesicles at short time (12–30 min postincubation) showing $p(\eta) = 2\eta$, ($r^2 = 0.9$ for a linear fit, ●); at intermediate times (30–45 min, ◇); and at long times (60–180 min, ○) and distribution of dextran (□) and LDL (△) containing vesicles at quasi-steady-state. (c) Immunolabeled microtubules (anti-α tubulin, [15]) with the nuclear and cell membranes superimposed. Arrow points towards the MTOC and (d) concentration of MTs in pixel intensity/ μm^2 (○) and concentration of PEI-DNA vesicles in #/ μm^2 (●) as a function of distance from the nuclear membrane.

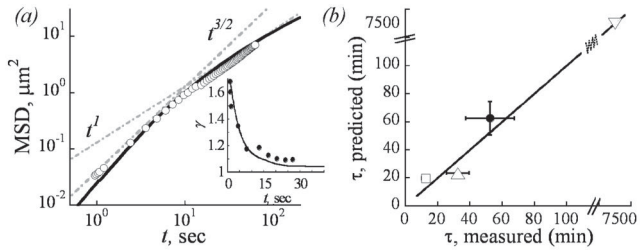

FIG. 5. (a) Average mean squared displacement for simulated trajectories (solid line) and the experimentally measured trajectories (○). A clear crossover from the sub-ballistic to diffusive regime occurs between $t = 10$–100 sec. See Ref. [9] for a discussion of MSD at very short time scales ($t < 1$). Inset: Variation of γ, (where MSD $\sim t^{\gamma}$) with t for measured trajectories (●) and simulated trajectories (solid line). (b) Comparison of predicted and observed time required for 95% equilibration for dextran (□), LDL (△), and PEI-DNA (●). In the presence of nocodazole (▽), a microtubule-destabilizing drug, t approaches infinity, calculated here by assuming $D^{\text{eff}} = D_0 = 10^{-3}\ \mu\text{m}^2/\text{sec}$.

bidirectional ballistic runs and pauses, and exhibits a diffusionlike behavior. Over a period of 1–25 sec, the experimentally measured exponent of time, γ, decreases monotonously from ~1.8 to 1 (Fig. 5, inset), showing progressive transformation from ballistic to diffusive motion. The crossover time is related to the time it takes for a vesicle to undergo several distinct ballistic runs and can be estimated by the time to complete one cycle of binding/unbinding [8]. Interestingly, $t^{3/2}$ scaling has also been observed in other unrelated systems but has been attributed to different physical mechanisms [11,12].

The long time ($t > 10$ sec) effective diffusion coefficient, D^{eff} can be theoretically related to short time ($t <$ 10 sec) ballistic parameters [8], $D^{\text{eff}} = \frac{(D_0 + 2K v^2/k')}{2K+1} \approx f\frac{v^2}{k'}$. D^{eff} can now be predicted using the parameter values measured for all three markers (Table I). These values of D^{eff} are typically 100-fold higher than vesicle's thermal diffusivity D_0. Consequently, vesicles rapidly disperse along the MTs, and the initial linear gradient of $p(\eta, t)$ is removed. The time required to complete ≈ 95% of equilibration is $\tau = L^2/4D^{\text{eff}}$, where L is the mean length of MTs, or the mean radius of the cells. A comparison of predicted time of equilibration (95%) with experimentally observed times is shown in Fig. 5(b). The differences in τ for three markers arise from a combination of differences in their sizes and/or due to differences in their mobile fractions (cf. Table I). It is possible that interactions between the marker and the vesicle influence the rate of binding of the motor-vesicle complex to MT, and consequently alter the trafficking rate of endosomes.

In summary, the measurements presented here demonstrate a simple principle by which the cells achieve and maintain an apparently asymmetric organization of endocytic vesicles on a time scale of 10–60 min. Two important aspects of the principle are (i) symmetric, bidirectional MT-based transport that translates to facilitated diffusion at long time scales and (ii) confined 1D motion on asterlike assembly of the MTs. It is now possible to predict the evolution of intracellular distribution of vesicles based only upon measurement of transport properties and the cell shape.

We argue that a well-defined distribution of endocytic vesicles is crucial to mixing and segregation of vesicle content, which in turn, is critical to delivery and processing of internalized material and transport of signals. Symmetric bidirectional transport provides a robust and rapid mechanism to establish such a distribution regardless of frequent perturbations in operating environments, such as cell motion and changing endocytic loads. It remains to be seen whether symmetric bidirectional movements are generic to all organelles. Other entities like mitochondria, lipid granules, and viruses have been shown to exhibit visibly biased directional transport [13,14], which leads to highly asymmetric distribution. It should be noted, nevertheless, that the asymmetry seen in distribution of early endocytic vesicles is inherent in the shape and organization of the cell, and must be considered while examining the spatial organization of all intracellular entities.

This work was supported by the University of California Biotechnology Program.

*Corresponding author.
Electronic address: samir@engineering.ucsb.edu

[1] J. Gruenberg, Nat. Rev. Mol. Cell Biol. **2**, 721 (2001).
[2] E. Daro, P. van der Sluijs, T. Galli, and I. Mellman, Proc. Natl. Acad. Sci. U.S.A. **93**, 9559 (1996).
[3] W. H. Lewis, Bull. Johns Hopkins Hospital **49**, 17 (1931).
[4] B. Herman and D. Albertini, J. Cell Biol. **98**, 565 (1984).
[5] M. A. Welte, Curr. Biol. **14**, R525 (2004).
[6] N. Hirokawa, Science **279**, 519 (1998).
[7] F. Nedelec, T. Surrey, and A. C. Maggs, Phys. Rev. Lett. **86**, 3192 (2001).
[8] D. A. Smith and R. M. Simmons, Biophys. J. **80**, 45 (2001).
[9] See EPAPS Document No. E-PRLTAO-95-068542 for a 10-page document. This document can be reached via a direct link in the online article's HTML reference section or via the EPAPS homepage (http://www.aip.org/pubservs/epaps.html).
[10] S. P. Gross, M. A. Welte, S. M. Block, and E. F. Wieschaus, J. Cell Biol. **148**, 945 (2000).
[11] A. Caspi, R. Granek, and M. Elbaum, Phys. Rev. Lett. **85**, 5655 (2000).
[12] X. L. Wu and A. Libchaber, Phys. Rev. Lett. **84**, 3017 (2000).
[13] M. A. Welte, S. P. Gross, M. Postner, S. M. Block, and E. F. Wieschaus, Cell **92**, 547 (1998).
[14] R. L. Morris and P. J. Hollenbeck, J. Cell Sci. **104**, 917 (1993).
[15] T. Mitchison and A. Desai, in iProtocol.mit.edu.